Shock compression of strongly correlated oxides: A liquid-regime equation of state for cerium(IV) oxide

Philippe F. Weck, Kyle R. Cochrane, Seth Root, J. Matthew D. Lane, Luke Shulenburger, John H. Carpenter, Travis Sjostrom, Thomas R. Mattsson, and Tracy J. Vogler

Phys. Rev. B **97**, 125106 — Published 5 March 2018

DOI: 10.1103/PhysRevB.97.125106

Shock compression of strongly-correlated oxides: A liquid-regime equation of state for cerium(IV) oxide

Philippe F. Weck,[1, *] Kyle R. Cochrane,[1] Seth Root,[1] J. Matthew D. Lane,[1] Luke Shulenburger,[1]
John H. Carpenter,[1] Travis Sjostrom,[2] Thomas R. Mattsson,[1] and Tracy J. Vogler[3]
[1]*Sandia National Laboratories, Albuquerque, NM 87185, USA*
[2]*Theoretical Division, Los Alamos National Laboratories, Los Alamos, NM 87545, USA*
[3]*Sandia National Laboratories, Livermore, CA 94551, USA*
(Dated: February 21, 2018)

The shock Hugoniot for full-density and porous CeO_2 was investigated in the liquid regime using *ab initio* molecular dynamics (AIMD) simulations with Erpenbeck's approach based on the Rankine-Hugoniot jump conditions. The phase space was sampled by carrying out NVT simulations for isotherms between 6,000 and 100,000 K and densities ranging from $\rho = 2.5$ to 20 g/cm^3. The impact of on-site Coulomb interaction corrections $+U$ on the equation of state (EOS) obtained from AIMD simulations was assessed by direct comparison with results from standard density functional theory simulations. Classical molecular dynamics (CMD) simulations were also performed to model atomic-scale shock compression of larger porous CeO_2 models. Results from AIMD and CMD compression simulations compare favorably with Z-machine shock data to 525 GPa and gas-gun data to 109 GPa for porous CeO_2 samples. Using results from AIMD simulations, an accurate liquid-regime Mie-Grüneisen EOS was built for CeO_2. In addition, a revised multiphase SESAME-type EOS was constrained using AIMD results and experimental data generated in this work. This study demonstrates the necessity of acquiring data in the porous regime to increase the reliability of existing analytical EOS models.

PACS numbers:

I. INTRODUCTION

Cerium(IV) oxide, CeO_2, is an important functional material in a broad range of technological applications, such as fuel cells,[1–3] catalysts,[4–8] gas sensors,[9] and polishing materials,[10] or luminescent materials.[11,12] This stems in part from its high oxygen mobility and storage capacity, superior physicochemical stability, and peculiar optical properties. While most of its applications are typically limited to moderate pressure and temperature, CeO_2 also serves as an archetypal f-electron system to study pressure-induced phase transformations and metallization in strongly-correlated fluorite-type (CaF_2) oxides under extreme conditions.[13–19] Computational and experimental high-pressure/high-temperature investigations of CeO_2 are valuable for gaining fundamental insights into the intricate nature of f-electron localization/delocalization ambivalence under changing local coordination environment in f-element systems.[20]

Previous computational studies demonstrated the importance of high-fidelity density functional theory (DFT) simulations to correctly analyze high-pressure experiments.[21,22] However, an accurate description of the electronic structure and properties of Ce^{3+}/Ce^{4+} oxides at low temperature remains challenging within the framework of standard DFT. For example, strongly correlated materials with narrow energy bands, such as f-bands of lanthanides and actinides and d-bands of transition metals are incorrectly represented by standard DFT, because of its unphysical description of Coulomb self-interaction.[23] Although the insulating character of CeO_2 with unoccupied $4f$ states is correctly reproduced with standard DFT, conventional local density approximation (LDA)[24] and generalized gradient approximation (GGA)[25] functionals underestimate its wide $O(2p)-Ce(5d)$ band gap.[26] Additionally, standard DFT incorrectly predicts cerium(III) oxide to be metallic,[26,27] while experiments show antiferromagnetic Mott-Hubbard insulator characteristics with a localized $4f$ occupied band in the $O(2p)-Ce(5d)$ energy gap.[28]

Recently, several theoretical extensions to standard DFT have attempted to address strongly correlated systems. These include DFT with on-site Coulomb interaction corrections (DFT+U),[29,30] self-interaction correction (SIC-DFT),[24] dynamic mean field theory (DFT+DMFT),[31] single-particle Green's function and screened Coulomb interaction approximation (GW),[32] and hybrid functionals based on screened Coulomb potentials.[33,34] Although many of these methods have yielded promising results for Ce^{3+}/Ce^{4+} oxides,[26,35–39] DFT+U remains a pragmatic choice to model cerium oxides, due to its simplicity, effectiveness, and relatively low computational cost – especially for CPU-intensive *ab initio* molecular dynamics (AIMD) simulations.

In this work, an equation of state (EOS) for full-density and porous CeO_2 in the liquid regime is derived from AIMD simulations using Erpenbeck's approach based on the Rankine-Hugoniot jump conditions[40]. The AIMD results are compared to shock compression experiments on porous CeO_2 using Sandia's Z-machine and to prior shock data from gas-gun and explosive drive experiments. The phase space was sampled by running AIMD simulations with fixed number of particles, volume and temperature (NVT) for isotherms between 6,000 and 100,000 K and densities ranging from $\rho = 2.5$ to 20 g/cm^3. The impact of on-site Coulomb interaction corrections $+U$ on the EOS obtained from AIMD simulations was assessed by comparison with standard DFT results. Classical molecular dynamics (CMD) simulations were also carried out using Sandia's LAMMPS code to model atomic-scale shock compression of larger porous CeO$_2$ models. Details of our computational and experimental approaches are given in Sec. II and III, followed by a discussion of our results in Sec. IV. A summary of our findings and conclusions is given in Sec. V.

II. COMPUTATIONAL METHODS

A. Ab initio molecular dynamics simulations

AIMD simulations were performed using spin-polarized DFT with Mermin's generalization to finite temperatures,[41] as implemented in the Vienna *Ab initio* Simulation Package (VASP, version 5.3.3).[42,43] The exchange-correlation energy was calculated using GGA,[25] with the Perdew, Burke, and Ernzerhof (PBE) parameterization,[44] which was utilized in previous CeO$_2$ studies and showed success for EOS work.[26,45–47] NVT simulations were performed at this level to calculate isotherms between 6,000 and 100,000 K and densities from 2.5 to 20 g/cm^3 in increments of 0.5 g/cm^3. This grid spacing was chosen as a balance between error introduced by bi-rational interpolation and AIMD computational time to generate each (P, T) point.

In addition to AIMD simulations with standard DFT (hereafter referred to as AIMD/PBE), AIMD/PBE+U simulations with an effective Hubbard parameter to account for the strong on-site Coulomb repulsion between localized Ce 4f electrons were carried out for selected isotherms. In the rotationally-invariant formalism developed by Dudarev*et al.*[30] a penalty functional is added to the standard DFT functional, E_{DFT}, that forces the on-site occupancy matrix in the direction of idempotency, *i.e.*

$$E_{\mathrm{DFT}+U} = E_{\mathrm{DFT}} + \frac{(\bar{U} - \bar{J})}{2} \sum_{\sigma} \left[\mathrm{Tr}(\rho^{\sigma}) - \mathrm{Tr}(\rho^{\sigma}\rho^{\sigma})\right], \tag{1}$$

where $\bar{U}$ and $\bar{J}$ are spherically-averaged matrix elements of the screened electron-electron Coulomb and exchange interactions, respectively, and ρ^{σ} is the density matrix of Ce 4f electrons with a given projection of spin σ. The fully-localized limit-like Dudarev's scheme was used for the double-counting correction. In Dudarev's approach only $U_{\mathrm{eff}} = \bar{U} - \bar{J}$ is meaningful. Similar to previous investigations of CeO$_2$,[26,48,49] a value of $U_{\mathrm{eff}} = 4.5$ eV, calculated using a self-consistent linear-response approach,[50] was adopted in PBE+U simulations reported in this study.

The interaction between valence electrons and ionic cores was described by the Projector Augmented Wave (PAW) method.[51,52] The Ce$(5s^2, 5p^6, 6s^2, 4f^1, 5d^1)$ and O$(2s^2, 2p^4)$ electrons were treated explicitly as valence states in the Mermin-Kohn-Sham (MKS) equations and the remaining core electrons together with the nuclei were represented by PAW pseudopotentials. The *GW* PAW pseudopotentials were used for Ce and O since they provide a superior description of conduction states sampled by AIMD simulations.[52,53] The plane-wave cutoff energy for the electronic wavefunctions was set to 800 eV, with partial occupancies for all bands controlled by Fermi-Dirac smearing, and stringent convergence settings necessary to analyze high-pressure experiments were imposed.[22,52–55]

A 72-atom supercell with periodic boundary conditions was used in the simulations to ensure that the interaction of molecular structures with their periodic images is negligible. Baldereschi's mean-value special k-point[56] was used for properties averaging in the Brillouin zone. Time step for ion-motion was set to 0.7 fs, with velocities scaled at each simulation step to the temperature, and each NVT simulation was run for $\simeq 3-8$ ps. Equilibration was achieved when the block average[57] of the standard deviation of the pressure was less than 0.5%.

The principal Hugoniot was computed with respect to the fluorite-type CeO$_2$ bulk structure (space group $Fm\bar{3}m$, IT No. 225) observed experimentally under ambient temperature and pressure conditions, with equilibrium lattice parameters $a_0 = 5.411 \pm 0.001$ Å, corresponding to an initial volume per atom of V_0=13.202 Å^3 and a density of ρ_0=7.216 g/cm^3.[35] The Hugoniot curve consists of the locus of all (P, V, T) points which satisfy the Hugoniot relation,

$$E - E_0 + (1/2)(P + P_0)(V - V_0) = 0, \tag{2}$$

where E is the specific internal energy, P is the pressure, $V = 1/\rho$ is the specific volume of shocked CeO$_2$ bulk, and E_0 and P_0 are the reference energy and pressure obtained from AIMD simulations at 300 K for the full-density fluorite-type CeO$_2$ structure. The Hugoniot points were calculated through a series of NVT simulations at multiple temperatures, for successive isotropically-compressed specific volumes from ambient to elevated pressure. For each specific volume, the Hugoniot state was obtained by interpolating the two (P, T) points which bracket the Hugoniot temperature and pressure. When solving the Rankine-Hugoniot relation for initially porous CeO$_2$, the full-density volume V_0 in Eq. (2) was replaced with the initial porous volume $V_{00} = 1/\rho_{00}$, while the reference energy E_0 and pressure P_0 of the full-density sample at ambient conditions were conserved.

B. Classical molecular dynamics simulations

CMD simulations were carried out using Sandia's LAMMPS code[58] to model atomic-scale shock compression of larger fully-dense and porous CeO$_2$ models. CMD has been used extensively to study shock compression mechanisms, which require the resolution of atomistic detail[59,60], and is especially useful when heterogeneity[61–63] requires domain sizes too large for AIMD simulations.

In this work, a rigid-ion potential developed by Cooper, Rushton, Grimes (CRG)[64] was utilized. The CRG potential is of the embedded atom method (EAM) form with added charge interactions. The potential is implemented in LAMMPS with a parameter set provided by the developers (see Appendix).

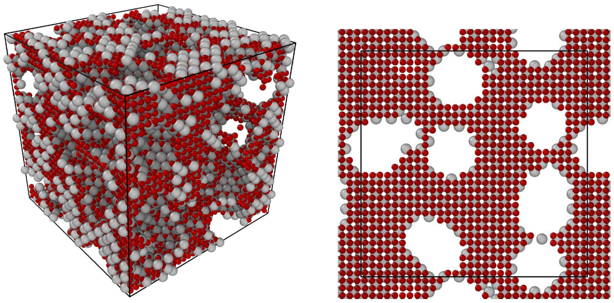

FIG. 1. (Color online) Porous CeO_2 model with initial density of $\rho_{00} = 4.0$ g/cm^3, featuring voids cut in a single crystal fluorite structure. (Left) A 3D rendering; (Right) a representative 0.4 nm slice. Color legend: O atoms, red; Ce atoms, grey.

The porous CeO_2 samples were produced by cutting voids from a pristine single crystal. Randomly placed 1.2 nm radius spherical voids were removed from a cubic fluorite sample with sides of length 8.123 nm and periodic boundaries in all dimensions. Only voids that maintained the system's neutral charge were allowed. After cutting, the system was equilibrated at 300 K and constant volume for 1 ns, followed by constant pressure of 1.0 atmosphere for an additional 1 ns. The final system had a density of 4.0 g/cm^3, and contained 22,602 atoms in an 8.084 nm cubic sample. The ambient density of CeO_2 at 1 atmosphere and 300 K was 7.197 g/cm^3 using the CRG potential. The simulation cell and a representative slice of the porous CeO_2 are shown in Figure 1.

Shocks were driven with the uniaxial constant-stress Hugoniostat method[65], which homogeneously compresses a system, while atoms are thermodynamically constrained to satisfy the Rankine-Hugoniot conditions. We have previously shown for comparable pressures in silicon, that the Hugoniostat gives identical final state Hugoniot results in porous compression studies[66].

Shock pressures ranged from a few GPa to over 250 GPa, using the LAMMPS shock extension package. Total simulation times were approximately 2 ns, with a damping parameter of 200 ps. A 0.2 fs time step was used in all simulations. Samples were pre-equilibrated to 300 K using a Langevin thermostat. System averages were calculated for density, pressure, and temperature. Here, and throughout this manuscript, pressure in CMD simulations refers to the 1D pressure in the propagation direction, *i.e.*, the P_{zz} component of the pressure tensor.

III. EXPERIMENTAL METHODS

To validate the AIMD and CMD methods, a series of shock compression experiments was conducted using Sandia's Z-machine[67,68]. The Z-machine is a pulsed power system capable of producing currents and magnetic fields up to 26 MA and 1000 T, respectively[69]. The combined current and magnetic field generates a Lorentz force ($\vec{F} = \vec{J} \times \vec{B}$) that can accelerate aluminum flyer plates up to 40 km/s[70]. Flyer plate experiments have been performed on Z for over a decade, with the methods continually being refined[70–72]. Shock compression experiments on Z have demonstrated consistent results with traditional gas-gun and explosively driven flyer plate methods for solids, aerogels, and liquids[22,73–75].

Figure 2 shows a schematic diagram of the Z experimental configuration. In the pressed density configuration, CeO_2 powder is pressed on a sapphire window to a defined thickness to make a sample with a density of approximately 4.0 g/cm^3. A metal drive plate, either Al or Cu, caps the powder, confining the powder between the sapphire window and the drive plate. Sample thicknesses are approximately 400 μm and 600 μm for the top and bottom samples, respectively. In the tap density configuration (Fig. 2, right), an aluminum drive plate is attached to a Lexan body. Quartz windows on the lexan body define the sample thicknesses at three locations: 350 μm, 500 μm, and 650 μm and the open volume between the Lexan body and aluminum cap is calculated. The volume was filled through fill holes on the top and bottom of the target and a vibration table was used to maximize the CeO_2 powder mass inside the cell. For both geometries, the initial density was calculated using the measured masses and volumes. For experiments with an initial density of ∼4 g/cm^3, 1 μm equiaxed CeO_2 provided by Anthony Fredenburg at Los Alamos National Laboratory was used. This material was from the same lot used in Refs. 16 and 17. For experiments conducted at ∼2.0 g/cm^3, CeO_2 from Atlantic Equipment Engineers with particles sizes ranging from 20 to 30 μm was used.

Both target geometries have quartz witness windows located above and below the CeO_2 sample locations. A velocity interferometer system for any reflector (VISAR)[76,77] was used to measure the flyer plate velocity up to impact on the witness windows. This provides impact velocities and impact times that are interpolated to determine the impact velocity and time at the sample locations. The transit time through the drive plate was calculated using the interpolated flyer plate velocity and the known Hugoniot for the flyer plate. Flyer plates and drive plates were either 6061-T6 aluminum or copper. VISAR was also used to measure the shock time of arrival at the powder sample – window interface. The transit time through the powder was calculated using the

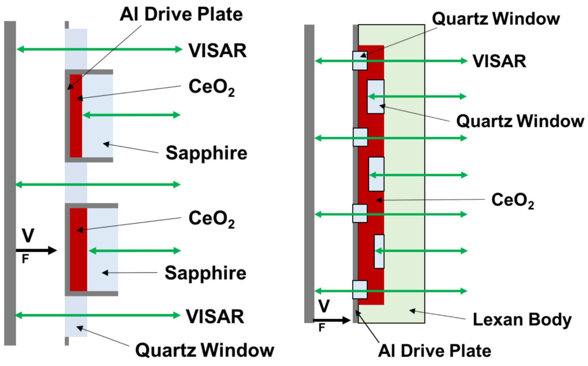

FIG. 2. (Color online) Illustration of the pressed density target geometry (left) used for the experiments with an initial density of $\sim$4.0 g/cm^3 and the tap density target geometry (right) for experiments with an initial density of $\sim$2.0 g/cm^3.

powder/window shock arrival time, the interpolated time of impact, and the transit time through the drive plate.

The CeO_2 shock velocity was calculated using the known powder thickness and transit time. To minimize heterogeneity effects from the powder samples, which may affect the Hugoniot state results, the weighted average of the shock velocity, U_s, was determined from the individual sample locations. The Hugoniot state was calculated using a Monte Carlo impedance matching method[78] that accounts for the uncertainties in the experimental measurements and the aluminum or copper Hugoniot.

IV. RESULTS AND DISCUSSION

Figure 3 shows the full-density CeO_2 EOS (ρ_0=7.216 g/cm^3) predicted from AIMD/PBE simulations along isotherms ranging from 6,000 to 100,000 K, with the corresponding principal Hugoniot. These AIMD/PBE simulations we carried out for ≈ 57M CPU hours using the high-performance computing platform Sequoia at Lawrence Livermore National Laboratory. Table I lists the Hugoniot states calculated using this level of theory. For comparison, Fig. 3 includes results from AIMD/PBE+U ($U_{\rm eff}$ = 4.5 eV) simulations along the 20,000 and 100,000 K isotherms. AIMD simulations at 300 K yielded reference mean energies and pressures of $E_0 = -8.666$ eV/atom and $P_0 = 7.544$ GPa for standard PBE ($U_{\rm eff}$ = 0.0 eV) and $E_0 = -8.127$ eV/atom and $P_0 = 9.850$ GPa for PBE+U ($U_{\rm eff}$ = 4.5 eV). Although the same theoretical full density for fluorite-type CeO_2 was used in both sets of AIMD simulations with standard DFT and DFT+U, the reference total energies and pressures differ as a result of the strong electron-electron repulsion included through the Hubbard correction term in Eq. (1). In Fig. 3(b), all energies from AIMD/PBE+U simulations were shifted by $\Delta E = -0.539$ eV to account for the difference in reference energies with AIMD/PBE results.

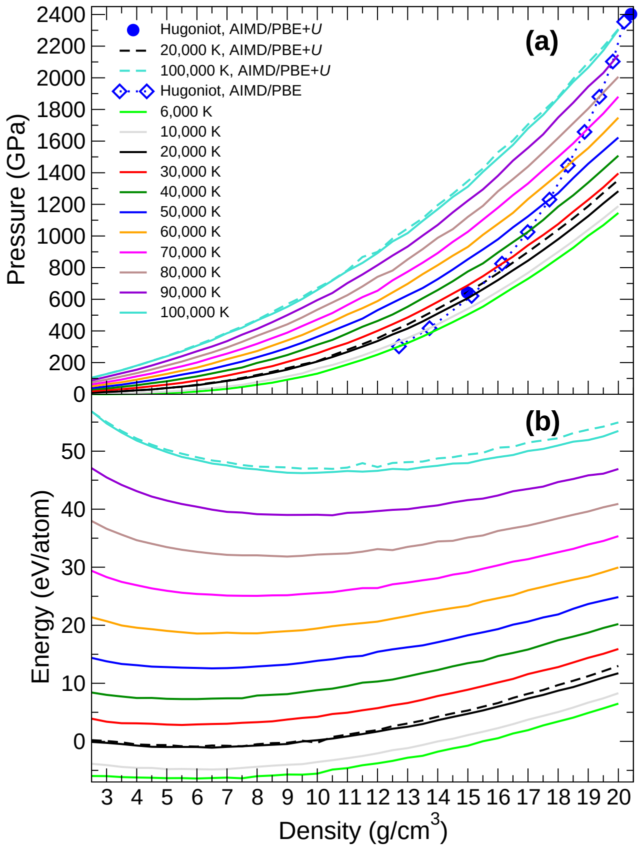

FIG. 3. (Color online) The CeO_2 (a) pressure and (b) specific internal energy as a function of density predicted from canonical AIMD/PBE simulations along isotherms between 6,000 and 100,000 K. The corresponding principal Hugoniot (ρ_0 = 7.216 g/cm^3) is depicted as a blue dotted curve in (a). Results from AIMD/PBE+U ($U_{\rm eff}$ = 4.5 eV) simulations along the 20,000 and 100,000 K isotherms (dashed lines) are also reported for comparison.

As shown in Fig. 3(a)–(b), results for the 20,000 and 100,000 K isotherms predicted from AIMD/PBE and AIMD/PBE+U simulations are in close agreement at low density. However, for densities above $\simeq$ 10 g/cm^3, AIMD/PBE+U systematically overestimate AIMD/PBE results, by up to $\simeq$ 6% in pressure and $\simeq$ 10% in energy at ρ = 20.0 g/cm^3 for the 20,000 K isotherm. AIMD/PBE+U results for the 100,000 K isotherm are larger than their AIMD/PBE counterparts by $\simeq$ 1% in pressure and $\simeq$ 3% in energy at ρ = 20.0 g/cm^3. This might stem from the fact that DFT+U imposes a static constraint on f-electron localization, even at high temperature and pressure, although under these conditions f electrons become more itinerant due to thermal broadening and owing to more efficient orbital overlap created by the external pressure. This is particularly true for most f-element oxides where f electrons are already on the brink of the localization-

TABLE I. Hugoniot states for CeO_2 with an initial solid density of 7.216 g/cm^3 calculated from canonical AIMD/PBE simulations along isotherms between 6,000 and 100,000 K.

T (K)	ρ (g/cm^3)	P (GPa)	u_p (km/s)	U_s (km/s)
6,000	12.714	302.4	4.257	9.844
10,000	13.729	417.5	5.239	11.04
20,000	15.125	621.3	6.710	12.83
30,000	16.135	825.2	7.951	14.38
40,000	16.987	1024.8	9.038	15.71
50,000	17.712	1230.3	10.05	16.96
60,000	18.325	1445.7	11.02	18.18
70,000	18.878	1657.8	11.91	19.28
80,000	19.368	1880.0	12.78	20.38
90,000	19.816	2102.7	13.61	21.41
100,000	20.192	2353.4	14.48	22.53

TABLE II. Hugoniot states for CeO_2 with an initial porous density of 2.0 g/cm^3 calculated from canonical AIMD/PBE simulations along isotherms between 6,000 and 100,000 K.

T (K)	ρ (g/cm^3)	P (GPa)	u_p (km/s)	U_s (km/s)
6,000	5.853	15.71	2.274	3.455
10,000	6.038	31.20	3.230	4.830
20,000	6.371	66.91	4.791	6.983
30,000	6.628	104.7	6.046	8.658
40,000	6.846	145.0	7.164	10.12
50,000	7.166	191.3	8.305	11.52
60,000	7.437	243.6	9.436	12.91
70,000	7.693	299.0	10.52	14.21
80,000	7.872	359.5	11.58	15.52
90,000	8.079	419.7	12.57	16.70
100,000	8.218	484.7	13.54	17.90

delocalization transition at ambient conditions and the f-electron delocalization pressure is typically well below 50 GPa.[20]

The principal Hugoniot points for full-density CeO_2 obtained by interpolating the (P,T) points bracketing the Hugoniot temperature and pressure are also shown in Fig. 3(a) for AIMD/PBE and AIMD/PBE+U simulations. The pressure for the Hugoniot state at 20,000 K (i.e. $P = 643$ GPa, $\rho = 15.0$ g/cm^3) is $\simeq 3-4\%$ larger for AIMD/PBE+U simulations than for AIMD/PBE (i.e. $P = 621$ GPa, $\rho = 15.1$ g/cm^3). At 100,000 K this difference between the Hugoniot states calculated with AIMD/PBE+U (i.e. $P = 2401$ GPa, $\rho = 20.4$ g/cm^3) and AIMD/PBE (i.e. $P = 2353$ GPa, $\rho = 20.2$ g/cm^3) reduces to only $\simeq 2\%$. Therefore, the $+U$ correction was found to have relatively limited impact on the simulated shock properties in the $P-T$ domain investigated here and only AIMD/PBE simulations are discussed in the remainder of this study.

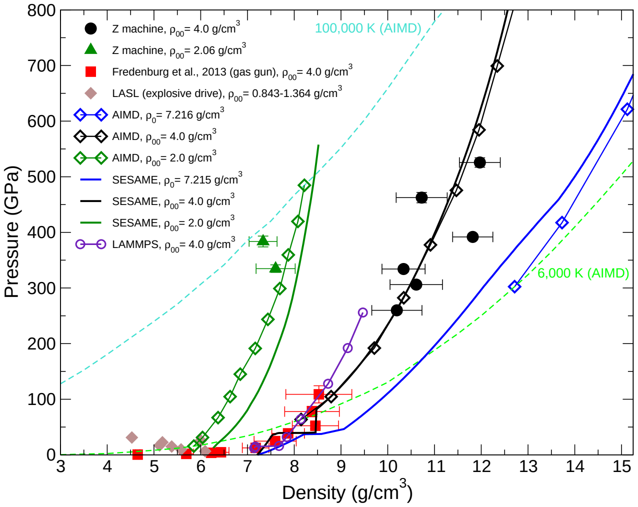

FIG. 4. (Color online) Hugoniot curves of fully-dense ($\rho_0 = 7.216$ g/cm^3) and porous ($\rho_{00} = 2.0$ and 4.0 g/cm^3) CeO_2 from canonical AIMD/PBE simulations between 6,000 and 100,000 K (isotherms are indicated by dashed lines). Z-machine data for $\rho_{00} = 2.06$ and 4.0 g/cm^3 and gas-gun data for $\rho_{00} \simeq 4.0$ g/cm^3 from Refs. [16 and 17] are plotted, along with the historical data from the LASL compendium [79] at $\rho_{00} = 0.843$ to 1.364 g/cm^3. The Hugoniot curves simulated using LAMMPS for $\rho_{00} \simeq 4.0$ g/cm^3 and SESAME EOS 96172 are also shown.

TABLE III. Hugoniot states for CeO_2 with an initial porous density of 4.0 g/cm^3 calculated from canonical AIMD/PBE simulations along isotherms between 6,000 and 100,000 K.

T (K)	ρ (g/cm^3)	P (GPa)	u_p (km/s)	U_s (km/s)
6,000	8.146	63.60	2.845	5.589
10,000	8.789	104.7	3.776	6.930
20,000	9.714	192.0	5.313	9.033
30,000	10.342	282.4	6.580	10.73
40,000	10.914	377.5	7.732	12.20
50,000	11.468	475.6	8.799	13.51
60,000	11.952	584.3	9.858	14.82
70,000	12.342	699.2	10.87	16.08
80,000	12.727	813.7	11.81	17.22
90,000	13.031	937.5	12.74	18.39
100,000	13.300	1064.6	13.64	19.51

The Hugoniot curves of porous CeO_2, with initial densities of $\rho_{00} = 2.0$ and 4.0 g/cm^3, derived from canonical AIMD/PBE simulations between 6,000 and 100,000 K are represented in Fig. 4, along with the AIMD/PBE principal Hugoniot; the Hugoniot states calculated at this level of theory are listed in Tables II and III for $\rho_{00} = 2.0$ and 4.0 g/cm^3, respectively. Porosity significantly affects the Hugoniot states, with the highest temperatures reached at relatively modest pressures for low initial densities. In particular, results obtained by solving the Rankine-Hugoniot relation for initially porous CeO_2 with ρ_{00}= 2.0 and 4.0 g/cm^3 are in good agreement with the Z-machine data. Table IV lists the Hugoniot states from the Z experiments. The AIMD/PBE results also agree with the gas-gun data from Fredenburg *et al.*[16] for CeO_2 powder samples with $\rho_{00} \simeq 4.0$ g/cm^3 at lower pressures. For the sake of completeness, historical explosive drive data from Ref. 79 for $\mathrm{CeO_2}$ with initial densities of $\rho_{00} \simeq 0.843$-1.364 g/cm^3 are displayed. Although a direct comparison between the present results and these low $P-T$ data is not straightforward, AIMD results for $\rho_{00}= 2.0$ g/cm^3 appear in fair agreement with these data down to 6,000 K, especially for densities in the vicinity of 6.0 g/cm^3.

The shock Hugoniot response of 4.0 g/cm^3 porous $\mathrm{CeO_2}$ in $P-\rho$ space calculated from CMD simulations using the CRG potential is also plotted in Figure 4. The predicted Hugoniot states are summarized in Table V. Above 16 GPa the samples became disordered. This onset of disorder correlates with a plateau at 16 GPa in the $P-\rho$ plot. It can be inferred that this plateau represents the onset of melting in the sample. The estimated temperature of this plateau is approximately 3,000 K. CMD results in the crush regime will be published elsewhere. In the solid phase regime, below 16 GPa, there are issues of strength which are beyond the scope of the results presented here. A similar study in silicon showed that at low pressures, the strength and P-V response is sensitive to the details of the pore structure.[80] Our emphasis in this work is on the liquid response regime.

At still higher pressures, significant heating is observed and the pressure increases with density. The ambient melt temperature of $\mathrm{CeO_2}$ is $\simeq 2,670$ K. The CMD simulated Hugoniot is in good agreement with experiments of Fredenburg *et al.* up to 109 GPa, as well as with AIMD Hugoniot states. Above this pressure, the CMD Hugoniot tends to differ significantly from the AIMD Hugoniot predictions, with a maximum deviation from AIMD results and Z data reached in the vicinity of 250 GPa. Such discrepancies might reflect some limitations of the CRG potential or CMD methodology in the high $P-T$ regime.

In addition, as shown in Fig. 4, Hugoniot curves for fully-dense and porous $\mathrm{CeO_2}$ ($\rho_{00} = 2.0, 4.0$ g/cm^3) were calculated using the solid-liquid SESAME 96172 EOS, constrained with the experimental and theoretical data reported in this study. SESAME 96172 EOS replaces the previous multiphase 96171 EOS[18,81] and has improvements in accuracy and predictiveness, and particularly so in the liquid regime. The EOS is based decomposing the free energy into zero temperature compression and thermal excitation components. Models are required for these components in order to span the wide ranges of temperatures and densities that are required for the EOS table. Each model contains various parameters that must be constrained by the limited amount of experimental or theoretical data. New automatic optimization procedures, such as particle swarm optimization[82], have been used to determine the final parameters, which provides a new level of accuracy. For the solid phases, new diamond anvil cell (DAC) data from Los Alamos National Laboratory has been obtained[19], which provides hydrostatic data for the EOS. The previous non-hydrostatic DAC results suffered from shear and strength influences that resulted in a stronger bulk modulus and reduced the solid-solid transition pressure. Additionally, the DAC work was performed at elevated temperatures up to 600 K, which provided constraint on the thermal expansion of the EOS. In the liquid regime we have relied on the extensive AIMD simulations of this study. The automatic optimization of the EOS parameters was used in determining the cold and thermal model parameters to provide good agreement over the entire range. A final shift in the energy was applied so the ambient pressure melt temperature was at the known value of $\simeq 2,670$ K. As shown in Fig. 4, both SESAME and AIMD Hugoniot results are in excellent agreement for ($\rho_{00} = 4.0$ g/cm^3), however, differences arise with decreasing temperature/pressure for both fully-dense and initially porous $\mathrm{CeO_2}$ with $\rho_{00} = 2.0$ g/cm^3. Such discrepancies stress the need to acquire additional data to increase the reliability of the EOS models.

The AIMD results contain inherent uncertainty that complicates the extraction of smooth derivatives of the energy and pressure through finite-difference methods. Accurate and smooth derivatives are needed to determine quantities such as sound speed, Grüneisen Γ, etc. An analytical EOS model was thus fit to the results to alleviate this issue. Due to the modest order-of-magnitude range of calculations, a simple polynomial model suffices. While such model is generally adequate for interpolation necessary to obtain smooth derivatives, let us note that fitting parameters will likely give poor extrapolations to zero pressure (i.e., where unconstrained, or when estimating higher derivatives) for comparison with independent measurements. The finite-strain approach developed by Birch for analyzing shock data at lower pressure should probably be better in terms of accuracy at low pressure.

The Helmholtz free energy is written as:

$$F(\rho,T) = f(T)\log\rho + g(\rho,T)\rho + h(\rho)T\log T + k(T). \quad (3)$$

The logarithmic terms are used to give the free energy a form that mimics an ideal gas, and f, g, h, and k are polynomials in their independent variables,

$$f(T) = \sum_{0\le i\le N} f_i \left(\frac{T}{T_0}\right)^i \quad (4)$$

$$g(\rho,T) = \sum_{0\le i+j\le N} g_{ij} \left(\frac{\rho}{\rho_0}\right)^i \left(\frac{T}{T_0}\right)^j \quad (5)$$

$$h(\rho) = \sum_{0\le i\le N} h_i \left(\frac{\rho}{\rho_0}\right)^i \quad (6)$$

$$k(T) = \sum_{0\le i\le N} k_i \left(\frac{T}{T_0}\right)^i \quad (7)$$

where ρ_0 and T_0 are arbitrary normalization constants to reduce the relative magnitudes of the polynomial coefficients and N is an integer which will be called the "order" of the EOS. This is simply a notational term, not a mathematically strict use. While the free energy could be written in a more compact form by combining

TABLE IV. The Z experimental parameters and the determined Hugoniot states.

Shot	Flyer / Drive Plate	V_F (km/s)	ρ_{00} (g/cm^3)	u_p (km/s)	U_s (km/s)	ρ (g/cm^3)	P (GPa)
Z3010 N	Al	18.74±0.08	2.07±0.05	10.85±0.11	14.91±0.22	7.602±0.418	334.8±6.8
Z3010 S	Al	20.20±0.08	2.05±0.07	11.61±0.14	16.12±0.18	7.334±0.299	383.6±9.7
Z2705 N	Al	12.94±0.08	4.05±0.05	6.22±0.08	10.32±0.24	10.195±0.537	259.9±4.6
Z2705 S	Al	14.35±0.08	4.01±0.05	6.89±0.09	11.08±0.24	10.610±0.561	306.1±5.1
Z2847 N	Al	15.08±0.07	3.97±0.05	7.20±0.08	11.69±0.22	10.338±0.461	334.1±4.9
Z2847 S	Al	16.69±0.09	4.04±0.04	7.99±0.08	12.14±0.15	11.818±0.430	391.8±4.9
Z2407 N	Cu	13.37±0.08	3.93±0.05	8.64±0.08	13.63±0.30	10.726±0.546	462.5±9.3
Z2407 S	Cu	14.64±0.08	3.91±0.06	9.51±0.08	14.13±0.18	11.970±0.437	525.6±8.5

TABLE V. Hugoniot states for CeO_2 with an initial porous density of 4.0 g/cm^3 calculated from LAMMPS/CRG simulations between 2,585 and 42,081 K.

T (K)	ρ (g/cm^3)	P (GPa)	u_p (km/s)	U_s (km/s)
2,585	7.142	12.0	1.150	2.613
2,882	7.169	15.0	1.287	2.912
2,912	7.676	16.0	1.384	2.889
4,790	7.840	32.0	1.980	4.042
8,431	8.139	64.1	2.854	5.612
18,176	8.725	127.9	4.160	7.683
29,509	9.145	192.0	5.196	9.236
42,081	9.468	255.9	6.078	10.524

the g and k terms, the above form explicitly calls out the separation of terms that occurs in the pressure.

The AIMD energy and pressure were fit to Eq. (3) by minimizing a least-squares objective. The energy was weighted using an absolute error of 1 MJ/kg and the pressure weighted by a relative error of 5%, except at 20 g/cm^3 where a 0.5% relative error was used to reduce spurious behavior of the polynomials at the highest densities. Coefficient values are listed in Table VI for three polynomial orders. While the 5th order polynomial had the lowest error when fit to the finite difference AIMD data, it produced unphysical oscillations. Therefore, the 4th order was used for subsequent curves and derivative values (see below).

To better understand the thermodynamics of the CeO_2 system, a modest range EOS was constructed using the Mie-Grüneisen EOS model. In many analytical models such as the Mie-Grüneisen EOS [see below Eqs. (8) through (12)], the governing parameters are often kept constant over the entire range of interest:

$$P = \frac{\rho_0 C_0^2 \chi \left[1 - \frac{\Gamma_0}{2}\chi\right]}{\left(1 - s_1\chi\right)^2} + \Gamma_0 E, \tag{8}$$

where E is the internal energy

$$E = \rho_0 \int C_v dT, \tag{9}$$

$$C_v = \left.\frac{\partial E}{\partial T}\right|_{\rho}, \tag{10}$$

$$\Gamma = \frac{1}{\rho}\left(\frac{\partial P}{\partial E}\right)_{\rho}, \tag{11}$$

$$\chi = 1 - \frac{\rho_0}{\rho}, \tag{12}$$

and C_0 and s_1 are linear fit parameters to the Hugoniot U_s *vs.* u_p data and C_v is the specific heat. C_0 varies with initial density and Γ_0 is Γ at ρ_0.

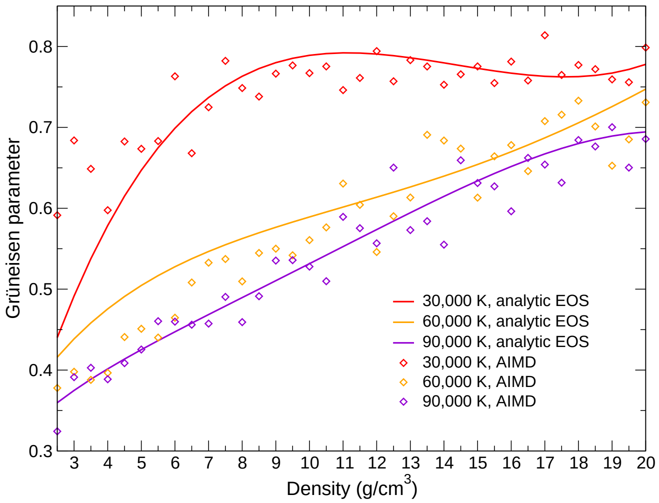

FIG. 5. (Color online) Evolution of the Grüneisen parameter, Γ, for CeO_2 calculated from Eq. (11) as a function of the density, along the 30,000, 60,000 and 90,000 K isotherms. Hollow diamonds represent the values calculated directly by finite-difference methods from the AIMD results. The solid lines correspond to the values obtained from the Mie-Grüneisen liquid model.

Using the AIMD-generated table, many of the assumptions utilized to build this type of EOS were tested. For

TABLE VI. Coefficients of the EOS models fit to the AIMD data. All coefficients have units consistent with the free energy F having units of MJ/kg.

N	3	4	5	N	3	4	5
f_0	1.411×10^{0}	1.828×10^{0}	1.973×10^{0}	h_0	-3.606×10^{-4}	-7.108×10^{-4}	-7.916×10^{-4}
f_1	-3.948×10^{-2}	-6.484×10^{-1}	-7.815×10^{-1}	h_1	-6.507×10^{-5}	-4.553×10^{-6}	-2.091×10^{-6}
f_2	1.460×10^{-1}	2.687×10^{-1}	2.885×10^{-1}	h_2	7.139×10^{-6}	3.472×10^{-6}	-2.585×10^{-7}
f_3	-1.780×10^{-3}	-9.401×10^{-3}	-1.284×10^{-2}	h_3	-1.807×10^{-7}	1.148×10^{-7}	2.269×10^{-7}
f_4		1.690×10^{-4}	4.144×10^{-4}	h_4		-1.531×10^{-8}	-1.408×10^{-8}
f_5			-6.381×10^{-6}	h_5			4.513×10^{-11}
g_{00}	-2.076×10^{0}	-1.993×10^{0}	-2.091×10^{0}	k_0	-9.072×10^{0}	-1.140×10^{1}	-1.180×10^{1}
g_{10}	3.871×10^{-1}	3.628×10^{-1}	3.976×10^{-1}	k_1	1.408×10^{3}	1.492×10^{3}	-9.984×10^{2}
g_{01}	2.230×10^{0}	1.008×10^{0}	1.019×10^{0}	k_2	-3.454×10^{-1}	1.082×10^{-1}	2.219×10^{-1}
g_{20}	-1.412×10^{-3}	3.847×10^{-3}	-6.976×10^{-3}	k_3	1.059×10^{-3}	-1.565×10^{-2}	-1.872×10^{-2}
g_{11}	-2.248×10^{-1}	-1.498×10^{-1}	-9.045×10^{-2}	k_4		2.656×10^{-4}	1.854×10^{-4}
g_{02}	-1.122×10^{-2}	-7.124×10^{-2}	-6.947×10^{-2}	k_5			4.566×10^{-6}
g_{30}	-5.607×10^{-4}	-9.861×10^{-4}	7.609×10^{-4}	g_{04}		-4.315×10^{-5}	-8.726×10^{-6}
g_{21}	6.094×10^{-3}	-1.147×10^{-3}	7.220×10^{-4}	g_{50}			5.122×10^{-6}
g_{12}	-1.514×10^{-5}	2.698×10^{-3}	5.420×10^{-3}	g_{41}			1.338×10^{-5}
g_{03}	2.589×10^{-4}	2.780×10^{-3}	2.223×10^{-3}	g_{32}			-2.670×10^{-7}
g_{40}		9.992×10^{-6}	-1.388×10^{-4}	g_{23}			3.599×10^{-6}
g_{31}		4.094×10^{-4}	-1.301×10^{-5}	g_{14}			7.729×10^{-7}
g_{22}		-5.955×10^{-5}	-1.679×10^{-4}	g_{05}			-4.857×10^{-7}
g_{13}		-4.991×10^{-5}	-1.495×10^{-4}				

example, physical parameters such as the Grüneisen Γ/V ratio, C_v, and C_0 are usually kept constant. First, Eq. (3) was used to obtain smooth derivatives. The error of the fits to the AIMD pressure were 1.1% 1.0% and 0.97% for $N = 3$, 4, and 5, respectively. The energy errors were 3.7, 2.5, and 1.9%. With the analytical free energy defined, the thermodynamic derivatives were calculated and compared to a simple finite-difference results for selected isotherms, as depicted in Figures 5 through 8.

The evolution of Γ as a function of the density is represented in Figure 5 along the 30,000, 60,000 and 90,000 K isotherms. The hollow diamonds are finite-difference values calculated directly from the AIMD results, while the lines are the derivatives of Eq. (3). Compared to finite-difference results, significantly smoother variations of Γ are predicted with the polynomial fit model. Figure 6 shows the Grüneisen Γ plotted as a function of pressure for isotherms ranging between 6,000 and 100,000 K. In the porous regime, Γ is a strong function of both density (pressure) and temperature. The downward curvature of the 100,000 K isotherm as pressure increases may be an artifact of the derivative along the edge of the AIMD-generated table. As discussed above, this simple polynomial model is expected to produce rather poor extrapolation at low pressure. Therefore, the curves shown in Figs. 5 and 6 may not correctly approach zero-pressure values but instead show an artificial drop toward an apparent (and incorrect) Grüneisen parameter of zero at zero pressure.

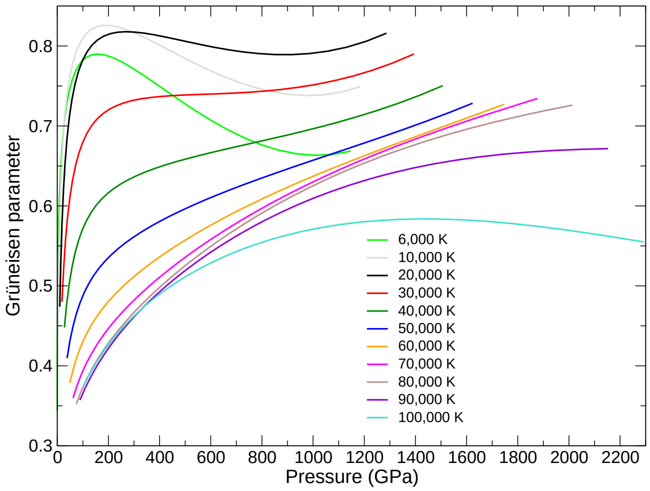

FIG. 6. (Color online) Evolution of the Grüneisen parameter, Γ, for CeO_2 calculated from Eq. (11) as a function of the pressure. This figure uses $N = 4$ from Table VI.

The variation of the specific heat, C_v, for the CeO_2 EOS grid is illustrated in Figure 7, along the 30,000, 60,000 and 90,000 K isotherms. As expected, the specific

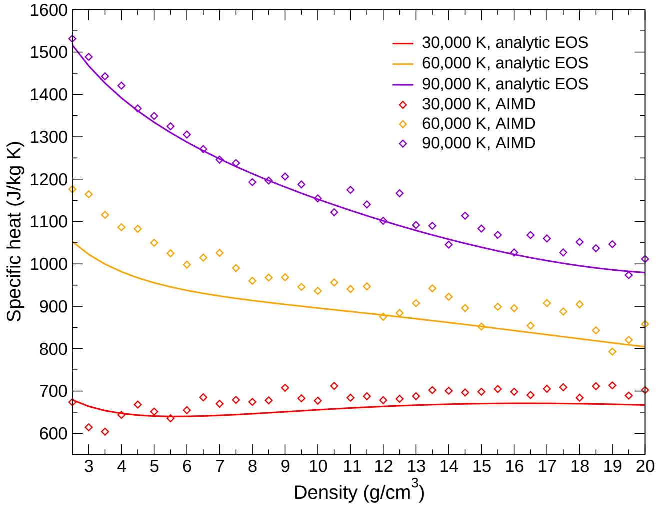

FIG. 7. (Color online) Specific heat, C_v, as a function of density along the 30,000, 60,000 and 90,000 K isotherms. Results calculated using a Mie-Grüneisen EOS (solid lines) and values computed directly from the AIMD-generated table (hollow diamonds) are represented.

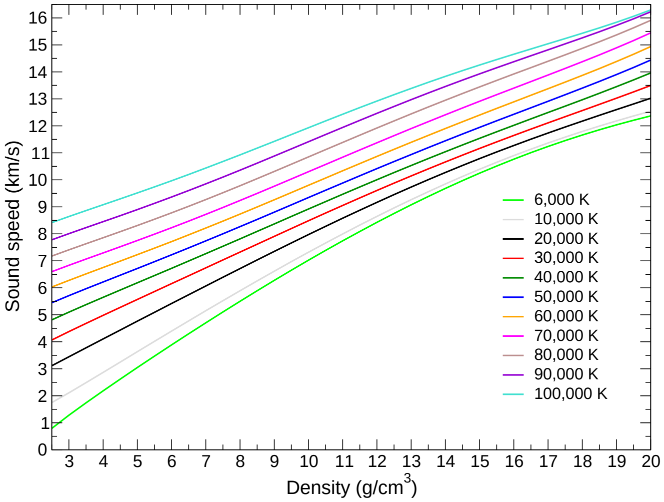

FIG. 8. (Color online) Variation of the sound speed for CeO_2 as a function of density, along isotherms between 6,000 and 100,000 K.

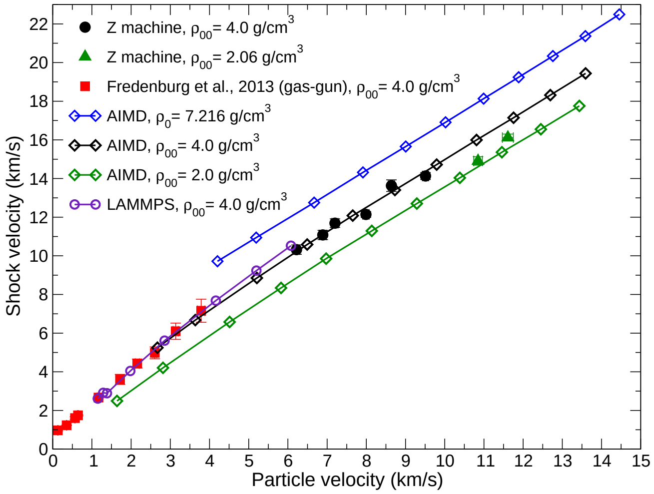

FIG. 9. (Color online) U_s *vs.* u_p for full-density ($\rho_0 = 7.216$ g/cm^3) and porous ($\rho_{00} = 2.0$ and 4.0 g/cm^3) CeO_2 from canonical AIMD/PBE simulations between 6,000 and 100,000 K. Z-machine data (this work) for samples with initial densities of $\rho_{00} = 2.06$ and 4.0 g/cm^3 and gas-gun data from Fredenburg *et al.* (Refs. [16 and 17]) for CeO_2 powder samples with $\rho_{00} \simeq 4.0$ g/cm^3 are also represented. Results from LAMMPS simulations for $\rho_{00} \simeq 4.0$ g/cm^3 (see Table V) are also displayed.

heat is primarily a function of temperature. At higher temperatures, where ionization is more prevalent, the specific heat decreases with density, owing to the mean free path of the electrons decreasing. Figure 8 displays the bulk sound speed as a function of density for temperatures in the range $6,000 - 100,000$ K. The bulk sound speed is calculated as

$$C_s^2 = \left.\frac{\partial P}{\partial \rho}\right|_s = \left.\frac{\partial P}{\partial \rho}\right|_T + \frac{\left(\left.\frac{\partial P}{\partial T}\right|_\rho\right)^2}{\rho^2 \left.\frac{\partial E}{\partial T}\right|_\rho} T \qquad (13)$$

Results show that the sound speed undergoes considerable variation over the EOS range investigated in this study.

u_p and U_s were computed from the AIMD-generated table. Based on the conservation equations, these velocities can be expressed as:

$$u_p = \sqrt{\frac{P - P_0}{\rho_0}} \sqrt{1 - \frac{\rho_0}{\rho}} \qquad (14)$$

and

$$U_s = \sqrt{\frac{P - P_0}{\rho_0}} / \sqrt{1 - \frac{\rho_0}{\rho}} \qquad (15)$$

Using the Hugoniot points from the Rankine-Hugoniot relation and the AIMD-generated table, the Hugoniot points were obtained in the $U_s - u_p$ representation along each isotherm (Figure 9). Taking the derivative of U_s with respect to u_p, a value of $s_1 \approx 1.25$ (Eq. 8) was calculated. The Mie-Grüneisen constants were subsequently checked using the information from AIMD simulations. Previous sound speed measurement for CeO_2 yielded a value of 4.95 km/s[83]. The specific heat C_v was estimated to be 356 J kg^{-1}K^{-1} and ρ_0=7.213 g/cm^3. We calculated

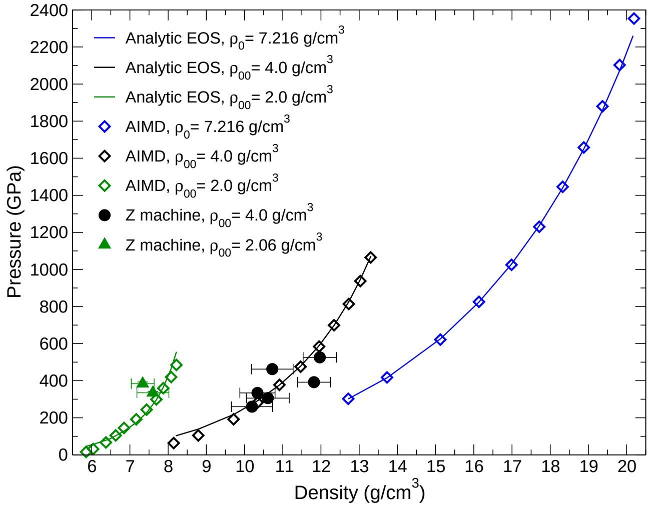

FIG. 10. (Color online) $P-\rho$ relationship along the principal and porous Hugoniots of CeO_2 for the AIMD-generated table (hollow diamonds), analytic EOS (solid lines), and Z-machine data (solid upper triangles and circles).

C_v using the formula:

$$C_v = C_p - \frac{T_0}{\rho_0}\eta^2 K_0, \tag{16}$$

where $C_p = 358$ J kg^{-1}K^{-1},[84,85] the bulk modulus is $K_0 = 220$ GPa,[13,35,86] the coefficient of thermal expansion is $\eta = 11 \times 10^{-6}$/K,[87] and $T_0 \approx 300$ K. Using C_v from Eq. (16), Γ was calculated according to the following expression:

$$\Gamma = \frac{\eta K_0}{C_v \rho} \approx 0.95 \tag{17}$$

Utilizing these parameters, a direct comparison was made between the Mie-Grüneisen results, the values computed from AIMD simulations, and the experimental data, as shown in Fig. 10. It was found that a shift of every 1% in s_1 added about 5% error between the principal Hugoniot results computed from the AIMD table and the Mie-Grüneisen principal Hugoniot values, with a noticeable change in the shape of the principal Hugoniot curve. When comparing the Mie-Grüneisen results to the shock data for $\rho_{00} \approx 4.0$ g/cm^3, the initial sound speed, C$_0$, needed to be adjusted to 2.79 km/s in order for the Mie-Grüneisen EOS to match values from the AIMD-generated table, which is in line with extrapolating to 300 K from Figure 8. Finally, C$_0$ was set to 1.172 km/s in order to match the 2 g/cm^3 porous data. In all three cases, s_1 was kept constant which is not a valid approximation for many materials.

V. CONCLUSION

The EOS for full-density and porous CeO_2 was investigated in the liquid regime, between 6,000 and 100,000 K and densities ranging from $\rho = 2.5$ to 20 g/cm^3, using *ab initio* molecular dynamics simulations within the framework DFT. Additional AIMD simulations were also carried out using DFT+U to assess the validity of standard DFT predictions. The impact of on-site Coulomb interaction corrections +U on the EOS and principal Hugoniot derived from AIMD simulations was found to be relatively limited, with pressure for Hugoniot states overestimating standard DFT predictions by $2-4\%$ within the $P-T-\rho$ domain investigated in this study. Results from AIMD compression simulations for porous Hugoniot with standard DFT are in good agreement with Z-machine shock data to 525 GPa and gas-gun data to 109 GPa for porous CeO_2 samples with initial densities of $\simeq 4.0$ g/cm^3.

In addition, classical molecular dynamics simulations were also conducted to model atomic-scale shock compression of larger porous CeO_2 models and test the potential impact of heterogeneity in domain sizes too large for AIMD simulations. The CMD simulated Hugoniot is in close agreement with gas-gun data and AIMD Hugoniot states to 109 GPa. Above this pressure, the CMD Hugoniot tends to increasingly deviate from both Z machine data and AIMD Hugoniot predictions up to 250 GPa. Such discrepancies might stem from limitations of the CRG potential or CMD methodology in the high $P-T$ regime.

The shock Hugoniots calculated from the AIMD table compared well with experimental data which gave confidence in the the table outside the regime covered by the experimental data. From those AIMD based Hugoniots, an accurate liquid-regime analytical (Mie-Grüneisen) EOS was built for CeO_2 across a broader range than available with experimental data. The AIMD table also allowed a better understanding of thermodynamic variables such as sound speed and specific heat. Because the finite differenced derivative terms are noisy, this was made easier by the polynomial liquid model fit to the AIMD table which smoothed the noise in the derivative terms. Finally, the findings discussed in this study demonstrate the necessity of acquiring data in the porous regime to increase the reliability of existing analytical EOS models. Further EOS development might be needed to improve agreement with the newly reported data for porous CeO_2.

Acknowledgments

Sandia National Laboratories is a multi-mission laboratory managed and operated by National Technology and Engineering Solutions of Sandia, LLC., a wholly owned subsidiary of Honeywell International, Inc., for the U.S. Department of Energy's National Nuclear Security

Administration under contract DE-NA0003525. T. S. acknowledges the support of the U.S. DOE/NNSA under Contract No. DE-AC52-06NA25396. We acknowledge Lawrence Livermore National Laboratory for access to the high-performance computing platform Sequoia and the Advanced Technology Computing Campaign (ATCC-3) for a generous CPU-time allocation. Anthony Fredenburg, Eric Chisolm and Scott Crockett (Los Alamos National Laboratory) are also acknowledged for useful discussions.

Appendix

The CRG potential is of the EAM form with added charge interactions. The rigid-ion potential is implemented in LAMMPS with a parameter set provided by the developers[64], as discussed below.

TABLE VII. Cooper, Rushton, Grimes potential parameters as reported in Ref. 64.

Parameter	O–O pair	Ce–Ce pair	Ce–O pair
$A_{\alpha\beta}$ (eV)	830.283	18 600	351.341
$\rho_{\alpha\beta}$ (Å)	0.3529	0.2664	0.3805
$C_{\alpha\beta}$ (eV Å^6)	3.8843	0.0	0.0
$D_{\alpha\beta}$ (eV)			0.7193
$\gamma_{\alpha\beta}$ (Å^{-1})			1.869
r_0 (Å)			2.356
G_α (eV Å$^{1.5}$)	0.690	0.308	
n_β (Å^5)	106.856	1556.803	

The form is given by:

$$E_i = \frac{1}{2}\sum_j \phi_{\alpha\beta}(r_{ij}) - G_\alpha \sqrt{\sum_j \sigma_\beta(r_{ij})}, \qquad (18)$$

where the first term is a pairwise interaction, and the second term is a many-body interaction. α and β represent atom species, and i and j label individual atoms.

The terms of the CRG potential are given by,

$$\begin{aligned}
\phi_{\alpha\beta}(r_{ij}) &= \phi_C(r_{ij}) + \phi_B(r_{ij}) + \phi_M(r_{ij}) \\
\phi_C(r_{ij}) &= \frac{q_\alpha q_\beta}{4\pi\epsilon_0 r_{ij}} \\
\phi_M(r_{ij}) &= D_{\alpha\beta}\left[exp(-2\gamma_{\alpha\beta}(r_{ij}-r_0))\right. \\
&\qquad \left. -\ 2\ exp\left(-\gamma_{\alpha\beta}(r_{ij}-r_0)\right)\right] \\
\phi_B(r_{ij}) &= A_{\alpha\beta}\ exp\left(\frac{-r_{ij}}{\rho_{\alpha\beta}}\right) - \frac{C_{\alpha\beta}}{r_{ij}^6} \\
\sigma_\beta(r_{ij}) &= \frac{n_\beta}{r_{ij}^8}
\end{aligned}$$

where $A_{\alpha\beta}$, $\rho_{\alpha\beta}$, $C_{\alpha\beta}$, $D_{\alpha\beta}$, $\gamma_{\alpha\beta}$, r_0, n_β and G_α are parameters given in Table VII.

---

[*] Email: pfweck@sandia.gov

[1] M. S. Dresselhaus and I. L. Thomas, Nature **414**, 332 (2001).

[2] G. A. Deluga, J. R. Salge, L. D. Schmidt, and X. E. Verykios, Science **303**, 993 (2004).

[3] S. Park, J. M. Vohs, and R. J. Gorte, Nature **404**, 265 (2000).

[4] D. Peer, J. M. Karp, S. Hong, O. C. Farokhzad, R. Margalit, and R. Langer, Nat. Nanotechnol. **2**, 751 (2007).

[5] C. Walkey, S. Das, S. Seal, J. Erlichman, K. Heckman, L. Ghibelli, E. Traversa, J. F. McGinnis, and W. T. Self, Environ. Sci.: Nano **2**, 33 (2015).

[6] A. Trovarelli and P. Fornasiero, *Catalysis by Ceria and Related Materials* (Imperial College Press, London, 2002).

[7] J. A. Rodriguez, S. Ma, P. Liu, J. Hrbek, J. Evans, and M. Pérez, Science **318**, 1757 (2007).

[8] Q. Fu, H. Saltsburg, and M. Flytzani-Stephanopoulos, Science **301**, 935 (2003).

[9] H. J. Beie and A. Gnorich, Sens. Actuators B **4**, 393 (1991).

[10] T. Hoshino, Y. Kurata, Y. Terasaki, and K. Susa, J. Non-Cryst. Solids **283**, 129 (2001).

[11] S. Mochizuki and F. Fujishiro, Phys. Status Solidi B **246**, 2320 (2009).

[12] A. Masalov, O. Viagin, P. Maksimchuk, V. Seminko, and I. Bespalova, J. Lumin. **145**, 61 (2014).

[13] S. J. Duclos, Y. K. Vohra, A. L. Ruoff, A. Jayaraman, and G. P. Espinosa, Phys. Rev. B **38**, 7755 (1988).

[14] L. Liu, H. X. Song, Z. Wang, H. Y. Geng, Q. Jing, Y. Zhang, S. Liu, S. Xiang, Y. Bi, J. Xu, Y. Li, X. Li, and J. Liu, J. Appl. Phys **112**, 013532 (2012).

[15] H. X. Song, L. Liu, H. Y. Geng, and Q. Wu, Phys. Rev. B **87**, 184103 (2013).

[16] D. A. Fredenburg, D. D. Koller, P. A. Rigg, and R. J. Scharff, Rev. Sci. Instrum. **84**, 013903 (2013).

[17] D. A. Fredenburg, D. D. Koller, J. D. Coe, and C. B. Kiyanda, J. Appl. Phys **115**, 123511 (2014).

[18] E. D. Chisolm, J. Phys.: Conf. Series **500**, 032004 (2014).

[19] M. K. Jacobsen, N. Velisavljevic, D. M. Dattelbaum, R. S. Chellapa, and C. Park, J. Phys.: Condens. Matter **28**, 155401 (2016).

[20] L. Petit, Z. Szotek, W. M. Temmerman, G. M. Stocks, and A. Svane, J. Nucl. Mater. **451**, 313 (2014).

[21] A. Mattsson, P. Schultz, M. Desjarlais, T. Mattsson, and K. Leung, Modelling and Simulation in Materials Science and Engineering **13**, R1 (2005).

[22] S. Root, R. J. Magyar, J. H. Carpenter, D. L. Hanson, and T. R. Mattsson, Phys. Rev. Lett. **105**, 085501 (2010).

[23] D. D. O'Regan, *Optimised Projections for the Ab Initio Simulation of Large and Strongly Correlated Systems* (Springer-Verlag, Berlin Heidelberg, 2012).

[24] J. P. Perdew and A. Zunger, Phys. Rev. B **23**, 5048 (1981).

[25] J. P. Perdew, J. A. Chevary, S. H. Vosko, K. A. Jackson,

M. R. Pederson, D. J. Singh, and C. Fiolhais, Phys. Rev. B **46**, 6671 (1992).

[26] J. L. F. Da Silva, M. V. Ganduglia-Pirovano, J. Sauer, V. Bayer, and G. Kresse, Phys. Rev. B **75**, 045121 (2007).

[27] G. Kresse, P. Blaha, J. L. F. Da Silva, and M. V. Ganduglia-Pirovano, Phys. Rev. B **72**, 237101 (2005).

[28] A. V. Prokofiev, A. I. Shelykh, and B. T. Melekh, J. Alloys Compd. **242**, 41 (1996).

[29] A. I. Liechtenstein, V. I. Anisimov, and J. Zaanen, Phys. Rev. B **52**, R5467 (1995).

[30] S. L. Dudarev, G. A. Botton, S. Y. Savrasov, C. J. Humphreys, and A. P. Sutton, Phys. Rev. B **57**, 1505 (1998).

[31] A. Georges, G. Kotliar, W. Krauth, and M. Rozenberg, Rev. Mod. Phys. **68**, 13 (1996).

[32] F. Aryasetiawan and O. Gunnarsson, Rep. Prog. Phys. **61**, 237 (1998).

[33] J. Heyd, G. E. Scuseria, and M. Ernzerhof, J. Chem. Phys. **118**, 8207 (2003).

[34] J. Heyd, G. E. Scuseria, and M. Ernzerhof, J. Chem. Phys. **124**, 219906 (2006).

[35] L. Gerward, J. S. Olsen, L. Petit, G. Vaitheeswaran, V. Kanchanad, and A. Svane, J. Alloys Compd. **400**, 56 (2005).

[36] D. Jacob, K. Haule, and G. Kotliar, Eur. Phys. Lett. **84**, 57009 (2008).

[37] P. J. Hay, R. L. Martin, J. Uddin, and G. E. Scuseria, J. Chem. Phys. **125**, 034712 (2006).

[38] J. Graciani, A. M. Marquez, J. J. Plata, Y. Ortega, N. C. Hernandez, A. Meyer, C. M. Zicovich-Wilson, and J. F. Sanz, J. Chem. Theory Comput. **7**, 56 (2011).

[39] J. Kullgren, C. W. M. Castleton, C. Muller, D. Munoz-Ramo, and K. Hermansson, J. Chem. Phys. **132**, 054110 (2010).

[40] J. J. Erpenbeck, Phys. Rev. A **46**, 6406 (1992).

[41] N. D. Mermin, Phys. Rev. **137**, A1441 (1965).

[42] G. Kresse and J. Hafner, Phys. Rev. B **47**, 558 (1993).

[43] G. Kresse and J. Furthmüller, Phys. Rev. B **54**, 11169 (1996).

[44] J. P. Perdew, K. Burke, and M. Ernzerhof, Phys. Rev. Lett. **77**, 3865 (1996).

[45] S. Fabris, S. de Gironcoli, S. Baroni, G. Vicario, and G. Balducci, Phys. Rev. B **71**, 041102(R) (2005).

[46] P. F. Weck and E. Kim, Phys. Chem. Chem. Phys. **18**, 26816 (2016).

[47] P. F. Weck, P. A. Juan, R. Dingreville, and E. Kim, J. Phys. Chem. C **121**, 14678 (2017).

[48] S. Fabris, S. de Gironcoli, S. Baroni, G. Vicario, and G. Balducci, Phys. Rev. B **72**, 237102 (2005).

[49] J. L. F. Da Silva, Phys. Rev. B **76**, 193108 (2007).

[50] M. Cococcioni and S. de Gironcoli, Phys. Rev. B **71**, 035105 (2005).

[51] P. E. Blöchl, Phys. Rev. B **50**, 17953 (1994).

[52] G. Kresse and D. Joubert, Phys. Rev. B **59**, 1758 (1999).

[53] P. E. Blöchl, Phys. Rev. B **50**, 17953 (1994).

[54] M. P. Desjarlais, Phys. Rev. B **68**, 064204 (2003).

[55] A. E. Mattsson, P. A. Schultz, M. P. Desjarlais, T. R. Mattsson, and K. Leung, Modelling Simul. Mater. Sci. Eng. **13**, R1 (2005).

[56] A. Baldereschi, Phys. Rev. B **7**, 5212 (1973).

[57] M. Allen and D. J. Tildesley, *Computer Simulations of Liquids* (Oxford Science Publications, 1987).

[58] S. J. Plimpton, J. Comp. Phys. **117**, 1 (1995), LAMMPS code, http://lammps.sandia.gov.

[59] H. B. L. and P. S. Lomdahl, Science **280**, 2085 (1998).

[60] K. Kadau, T. C. Germann, P. S. Lomdahl, and B. L. Holian, Science **296**, 1681 (2002).

[61] S. Traiviratana, E. M. Bringa, D. J. Benson, and M. A. Meyers, Acta Mater. **56**, 3874 (2008).

[62] J. M. D. Lane, G. S. Grest, and T. R. Mattsson, Comp. Mater. Sci. **79**, 873 (2013).

[63] S. Root, T. A. Haill, J. M. D. Lane, A. P. Thompson, G. S. Grest, D. G. Schroen, and T. R. Mattsson, J. Appl. Phys **114**, 103502 (2013).

[64] M. Cooper, M. Rushton, and R. Grimes, J. Phys.: Condens. Matter **26**, 105401 (2014).

[65] R. Ravelo, B. L. Holian, T. C. Germann, and P. S. Lomdahl, Phys. Rev. B **70**, 014103 (2004).

[66] J. M. D. Lane, A. P. Thompson, and T. J. Vogler, Phys. Rev. B **90**, 134311 (2014).

[67] R. B. Spielman *et al.*, in *Proc. 11th Intl. Conf. High-Power Particle Beams* (1996) p. 150.

[68] M. K. Matzen, Phys. Plasmas **4**, 1519 (1997).

[69] M. E. Savage *et al.*, in *2007 IEEE Pulsed Power Conference*, Vol. 1-4 (2007) p. 979.

[70] R. W. Lemke, M. D. Knudson, and J.-P. Davis, Int. J. Impact Engng. **38**, 480 (2011).

[71] R. W. Lemke, M. D. Knudson, C. A. Hall, T. A. Haill, M. P. Desjarlais, J. R. Asay, and T. A. Mehlhorn, Phys. Plasmas **10**, 1092 (2003).

[72] R. W. Lemke, M. D. Knudson, D. E. Bliss, K. Cochrane, J.-P. Davis, A. A. Giunta, H. C. Harjes, and S. A. Slutz, J. Appl. Phys. **98**, 073530 (2005).

[73] M. D. Knudson and M. P. Desjarlais, Phys. Rev. Lett **103**, 225501 (2009).

[74] M. D. Knudson and R. W. Lemke, J. Appl. Phys. **114**, 4817433 (2013).

[75] M. D. Knudson, R. W. Lemke, D. B. Hayes, C. A. Hall, C. Deeney, and J. R. Asay, J. Appl. Phys. **94**, 4420 (2003).

[76] L. M. Barker and R. E. Hollenbach, J. Appl. Phys. **43**, 4669 (1972).

[77] L. M. Barker and K. W. Schuler, J. Appl. Phys. **45**, 3692 (1974).

[78] S. Root, L. Shulenburger, R. W. Lemke, D. H. Dolan, T. R. Mattsson, and M. P. Desjarlais, Phys. Rev. Lett. **115**, 198501 (2015).

[79] S. P. Marsh, ed., *LASL Shock Hugoniot Data* (University of California Press, 1980) p. 658.

[80] J. M. D. Lane, A. P. Thompson, and T. J. Vogler, AIP Conference Proceedings **1793**, 120010 (2017).

[81] E. D. Chisolm, *SESAME 96170, A Solid-Liquid Equation of State for CeO_2* (Los Alamos National Laboratory, Technical Report LA-UR 12-21066, 2012).

[82] G. A. Cox and M. A. Christie, J. Phys.: Condens. Matter **27**, 405201 (2015).

[83] A. Nakajima, A. Yoshihara, and M. Ishigame, Phys. Rev. B **50**, 13297 (1994).

[84] E. F. J. Westrum and A. F. J. Beale, J. Phys. Chem. **65**, 353 (1961).

[85] R. J. M. Konings, O. Benes, A. Kovacs, D. Manara, D. Sedmidubsky, L. Gorokhov, V. S. Iorishc, V. Yungman, E. Shenyavskaya, and E. Osina, J. Phys. Chem. Ref. Data **43**, 013101 (2014).

[86] L. Gerward and J. S. Olsen, Powder Diffr. **8**, 127 (1993).

[87] S. Stecura and J. W. Campbell, *Thermal Expansion and Phase Inversion of Rare-Earth Oxides* (U.S. Department of the Interior, Bureau of Mines, Report 5847, 1961).